ACS OMEGA

Open Access

http://pubs.acs.org/journal/acsodf

Article

Effect of Low to High Pressure on the Structural, Mechanical, Electrical, and Optical Properties of Inorganic Material Ca_3AsBr_3: An Ab Initio Investigation

Md. Arif Ul Islam,* Ovijit Das, Dev Bahadur Khadka, Md. Rasidul Islam, Md. Ferdous Rahman, Shinya Kato, and Tetsuo Soga

Cite This: *ACS Omega* 2024, 9, 8005−8018

Read Online

ACCESS | Metrics & More | Article Recommendations | Supporting Information

ABSTRACT: Inorganic metal halide solar cells made from perovskite stand out for having outstanding efficiency, cheap cost, and simple production processes and recently have generated attention as a potential rival in photovoltaic technology. Particularly, lead-free Ca_3AsBr_3 inorganic materials have a lot of potential in the renewable industry due to their excellent qualities, including thermal, electric, optoelectronic, and elastic features. In this work, we thoroughly analyzed the stress-driven structural, mechanical, electrical, and optical properties of Ca_3AsBr_3 utilizing first-principles theory. The unstressed planar Ca_3AsBr_3 compound's bandgap results in 1.63 eV, confirming a direct bandgap. The bandgap within this compound could have changed by applying hydrostatic stress; consequently, a semiconductor-to-metallic transition transpired at 50 GPa. Simulated X-ray diffraction further demonstrated that it maintained its initial cubic form, even after external disruption. Additionally, it has been shown that an increase in compressive stress causes a change of the absorption spectra and the dielectric function with a red shift of photon energy at the lower energy region. Because of the material's mechanical durability and increased degree of ductility, demonstrated by its stress-triggered mechanical characteristics, the Ca_3AsBr_3 material may be suitable for solar energy applications. The mechanical and optoelectronic properties of Ca_3AsBr_3, which are pressure sensitive, could potentially be advantageous for future applications in optical devices and photovoltaic cell architecture.

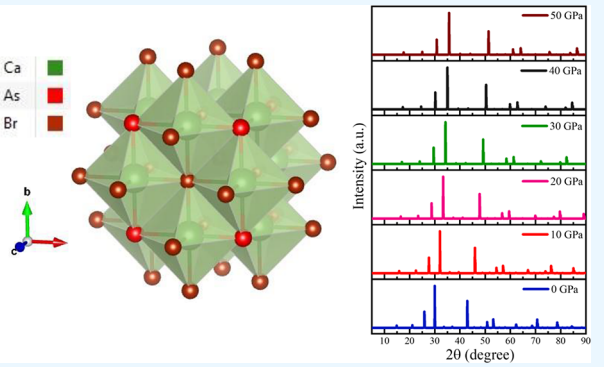

1. INTRODUCTION

Environmental concerns around the world and rising demand for energy, along with the continuous advancement in technologies for renewable energy, encourage the use of renewable energy sources. Solar energy is among the most inexpensive and plentiful of all the long-term natural resources currently. The solar photovoltaic (PV) technique is among the most efficient methods to harness the power of sunlight to produce electricity by converting sunlight into direct currents within solar cells (also known as PV cells). Perovskite-based materials provide a variety of exciting advantages in solar cell technology.[1] This is why they are now the subject of intense research and development worldwide. In the past, this term was used to describe metal oxides with perovskites, which are generally classified as piezoelectric or ferroelectric materials.[2] Perovskites made from inorganic materials are often produced for use in a variety of photoelectric and energy-related purposes.[3−5] For instance, solar cells,[3,6] light-emitting diodes,[7,8] and equipment for converting renewable energy. The ability of halide type perovskites to produce light in light-emitting diodes (LEDs) was discovered by Mitzi's group in the 1990s,[9−11] and recently related LEDs have been produced.[12,13]

In spite of the fact that the process of converting light into electricity is the opposite of that of converting electricity into light, the first paper on halide perovskites being used as photovoltaic solar absorbers appeared a few decades after the first article on electricity into light.[14] A rapid rise in power conversion efficiency (PCE) from 3.8% to more than 25% in less than a decade has attracted significant attention for organic−inorganic hybrid perovskite solar cells.[15] Recently, solar panel technology offered a tempting replacement for conventional sources of energy because of its highly effective transformation of light energy into electric power and minimal loss processes. The features of the perovskite materials have improved during the last ten years, speeding up this development.[5] In the green solar industry[16−19] it is also

Received: October 16, 2023
Revised: December 13, 2023
Accepted: December 14, 2023
Published: February 9, 2024

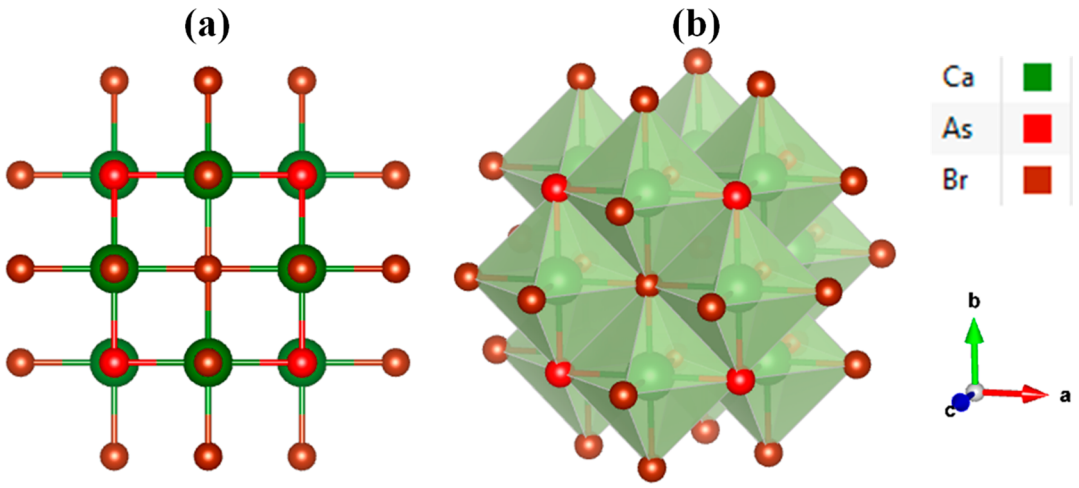

Figure 1. Constructed (a) two-dimensional (2D) and (b) three-dimensional (3D) crystals of the Ca_3AsBr_3 compound.

creating a lot of buzz. Pinhole-free homogeneous perovskite material to fabricate more solar modules that are more efficient, convenient, and safer with regard to the environment is a new era that researchers are eyeing.

The crystal structure as well as characteristics of perovskite materials may be changed to make them appropriate for optoelectronic devices using the powerful technique of stress-induced engineering.[20−23] According to recent studies on how stress affects material properties, there is a strong and visible relationship between the stress that is given to a material and its structural characteristics.[24,25] Hadenfeldt et al. conducted an experimental study, and the report also showed the possibility for utilizing it in thermal applications.[26] Stress causes the semiconductor to change from semiconductor to metallic, which increases the possibility of employing it in conducting applications.[27] The most important and practical method is to use pressure to adjust the optoelectronic, mechanical, and thermoelectric transport phenomena.[28−30] The alteration of these characteristics by octahedral shrink caused by hydrostatic pressure makes pressurized crystal seem superior to bare crystal.[31]

Inorganic compounds have gained prominence in photovoltaic technology due to their extensive structural, electronic, and optical properties. Recently, several studies examined different inorganic compounds, such as Ca_3AsI_3 and Sr_3AsCl_3. In a study published in 2023, Rahman et al. explored spin−orbit coupling and strain effects on Ca_3AsI_3, showing the bandgap of the material is 1.58 eV and that strain can vary the bandgap.[32] Rahman et al. also published a paper that year that examined Sr_3AsCl_3's strain-induced properties, revealing a direct bandgap of 1.649 and 2.473 eV for the Perdew−Berke−Enzerhof (PBE) and Heyd−Scuseria−Ernzerhof (HSE) functions and showing that compressive strain results in a blue shift in absorption spectra and dielectric function, whereas tensile strain results in a red shift.[33] The first investigation of Ca_3AsBr_3 conducted by Hadenfeldt et al. in 1984, the thermal behavior of the compound was studied, including phase transformations and heat absorption.[26] In our study of Ca_3AsBr_3, we examined the compound's structural, mechanical, electrical, and optical properties for the first time under stress, showing a direct bandgap of 1.63 eV and a transition from semiconductor to metal at 50 GPa. Additionally, the material has a high degree of ductility and mechanical durability, making it suitable for solar energy applications. When the stress is created from 0 to 50 GPa, for example, it considerably impacts the structural, mechanical, electrical, and optical characteristics of Ca_3AsBr_3 compound. To make Ca_3AsBr_3 appropriate for use in conducting applications, it is crucial to minimize its bandgap value while keeping it within a steady stability range suited for constructing flawless goods of any sort. There has not, however, been a thorough investigation of how stress impacts the optical, electrical, and mechanical characteristics of Ca_3AsBr_3. In this study, the electrical, optical, and mechanical aspects of Ca_3AsBr_3 are thoroughly investigated in relation to stress using Density Functional Theory, often known as DFT. We thoroughly examined the band structure and the procedure for modifying the Ca_3AsBr_3 bandgap. We looked at how the presence of external stress alters the physical properties, including electronic bandgap, to define the electric characteristics of Ca_3AsBr_3. Understanding elastic constants, anisotropy, and moduli is essential to appreciate a compound's potential for device construction applications fully.[34−36] On the other hand, the anticipated pressure-sensitive electrical and optical properties are crucial for comprehending the suitability of the investigated materials for optoelectronic applications.[37,38] A number of these aspects motivate us to do more theoretical research utilizing the ab initio density functional theory (DFT) procedure, a well-liked technique for forecasting new energy substances based on the electrical, mechanical, and optical properties of these compounds.

The challenges associated with its use as a solar cells' material should not be ignored, despite Ca_3AsBr_3's promising characteristics. In this study, while the material exhibits a direct bandgap and photoconductivity, we did not evaluate essential parameters such as carrier lifetime and diffusion length. In solar cell applications, these parameters play a vital role in determining a material's efficiency. A comprehensive analysis of carrier dynamics is needed to better understand and optimize the photovoltaic performance of Ca_3AsBr_3.

2. COMPUTATIONAL DETAILS

We used a ultrasoft pseudopotential in the setting of density-functional theory (DFT).[39] We used the Generalized Gradient Approximation (GGA) along with the PBE exchange-correlation interactions function to investigate the optoelectronic properties.[40] The density functional theory calculations were performed using the Cambridge Serial Total Energy

https://doi.org/10.1021/acsomega.3c08131
ACS Omega 2024, 9, 8005−8018

Package (CASTEP) program.[41−43] We established a kinetic energy cutoff of 600 eV in order to improve the simulation performance and structural optimization. A maximum allowable force tolerance was set at 0.01 eV for this computation analysis. We kept the self-consistent function boundary at roughly 10^{-6} atomic units to accurately simulate the ground state energy. We considered a convergence threshold of forces of 10^{-3} atomic units for structural characteristics and ionic relaxation. Additionally, we used a 15 × 15 × 15 Monkhorst−Pack[44] k-mesh grid to calculate the electronic band configuration and the density of states (DOS) by integrating over the first Brillouin zone.[45] The CASTEP package applies the finite theory of strain to calculate the elastic parameters.[46] The factors for geometry optimization convergent threshold include a maximum displacement of 0.0005, which is the highest stress of 0.02 GPa, maximum forces of 0.01 eV/Å, and overall energy of 1×10^{-6} eV/atom.[47] The optical properties obtained on the standard DFT Kohn−Sham orbits are subtracted using the CASTEP program.[48−50]

3. RESULTS AND DISCUSSION

3.1. Structural Properties. In the process-structure performance, the structure of the material correlates with every prospect in this hybrid regime. Ca_3AsBr_3 is a metal base halide containing a $Pm\bar{3}m$ cubic spacing group. There are seven atoms in total in a unit cell. Figure 1a depicts the crystalline structure of Ca_3AsBr_3, which crystallizes in the $Pm\bar{3}m$ spacing group. In this unit cell, the Ca atoms reside in the 3d Wyckoff site as well as (1/2, 0, 0) fractional coordinates. As atoms are in that 1a Wyckoff site, and (0 0, 0) fractional coordinates, Br atoms reside in the 3c Wyckoff site as well as (0, 1/2, 1/2) fractional coordinates. When Ca^{2+} forms bonds with two corresponding As^{3-} and four similar Br^{1-} atoms, $CaAs_2Br_4$ octahedra are formed with sharing to their corners and outside edges. There is no inclination at all in the shared corner octahedra. As^{3+} forms corner-sharing $AsCa_6$ octahedra by forming covalent bonds with six different Ca^{2+} molecules. There is no distortion in the two nearby octahedra. In an alternating square arrangement, the Br^{1-} ion is joined to four comparable Ca^{2+} molecules. Binding energy fluctuation with an alteration in its lattice constant has been seen by utilizing relax processing in a PBE program, allowing parameters of structure-like lattice constants to be determined. By assessing the lattice constant, the quantity that yields the ground state's lowest energy intensity, and maintaining the structural integrity of the lattice structure, the energetic density function of the fundamental state is easy to calculate. The lattice parameter of our ideal relaxing Ca_3AsBr_3 arrangement is 5.95. The optimal number agrees well with earlier studies.[26] As a result, the two- and three-dimensional perspectives of the Ca_3AsBr_3 lattice framework are graphically shown in Figure 1a and b. The sections that follow will go through the electrical and optical characteristics that may be obtained by this form of hypostatic stress integration.

The lattice constants and the volume of a crystal decrease with pressure, as can be seen in Figure 2, because the atoms are pushed closer together. The reason for this is that the external pressure forces the atoms over their repelling forces, and they occupy an area that is smaller. In Figure 3, simulated X-ray diffraction (XRD) analysis is illustrated.[51] It is evident from XRD analysis that the sample is cubic (JCPDS card no. 04−010−0309),[26] and maintained its cubic property even after applying stress ranging from 0 to 50 GPa. Due to pressure, the

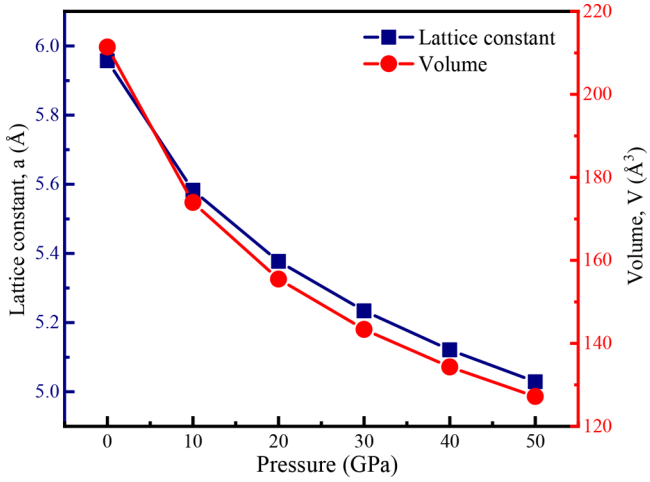

Figure 2. Variation of the lattice constant and volume as a function of pressure.

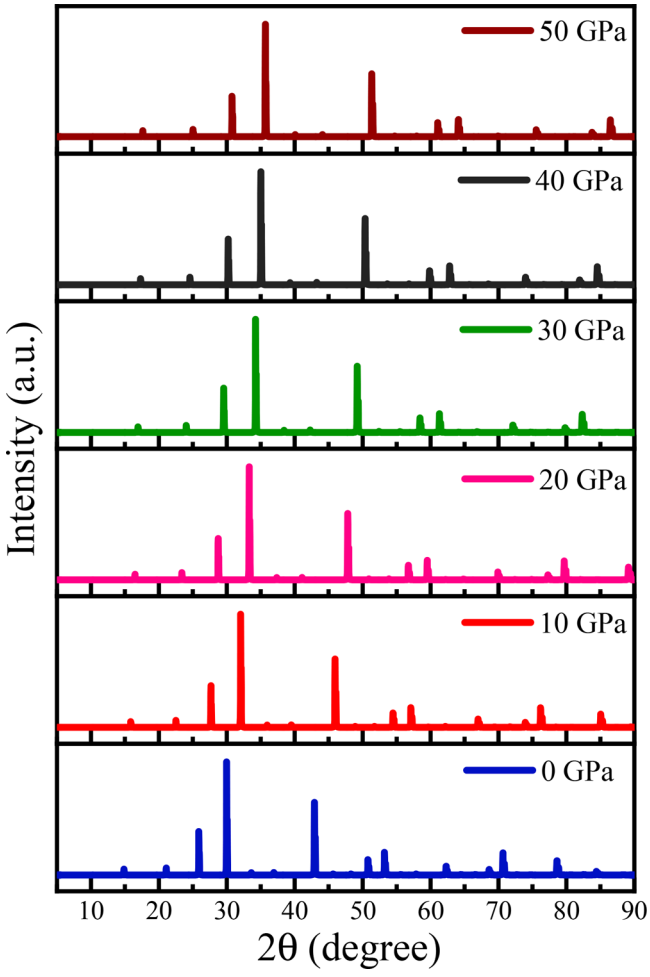

Figure 3. Simulated XRD signature of the Ca_3AsBr_3 compound at various pressures.

peaks shift to the right side without changing their original structure. Figure 2 depicts that with more induced pressure, the lattice constant and the lattice volume decrease. The XRD peaks shift toward the right with increased pressure; this indicates that the lattice constants of Ca_3AsBr_3 material are decreased. As previously mentioned, adding pressure to

https://doi.org/10.1021/acsomega.3c08131
ACS Omega 2024, 9, 8005−8018

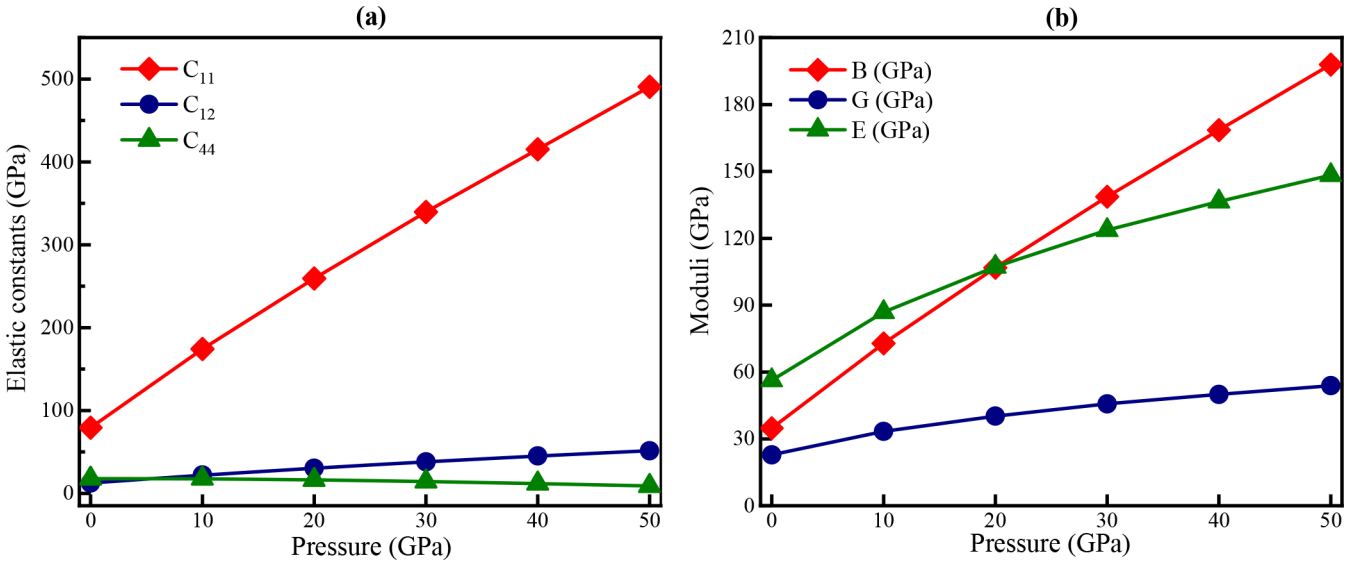

Figure 4. Estimated (a) elastic constants and (b) elastic moduli with respect to pressure for Ca_3AsBr_3.

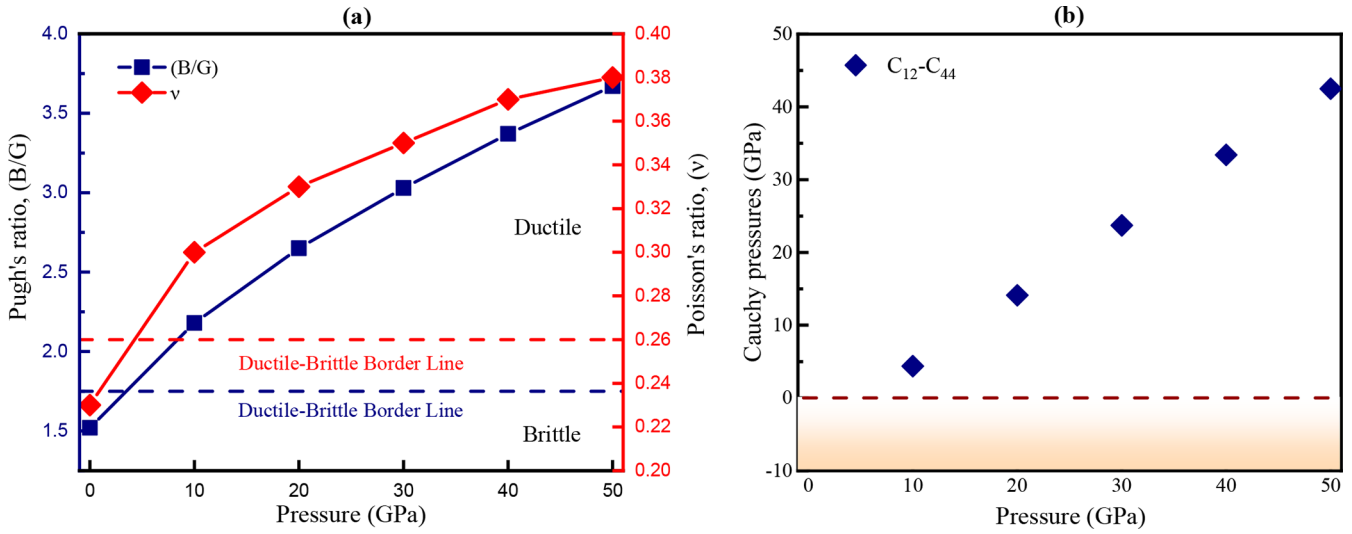

Figure 5. Estimated (a) Pugh's and Poisson's ratios and (b) Cauchy pressures with respect to pressure for Ca_3AsBr_3.

compound can force particles closer to each other, which reduces the lattice constant.

3.2. Mechanical Properties. The elastic parameters for the metallic halide Ca_3AsBr_3 were calculated because they provide information on the crystal's sensitivity to various stresses ranging from 0 to 50 GPa. The constants of elasticity may also be used to determine a material's stiffness and stability.[52,53] The dynamical information on the resistance of a substance to external pressure may also be calculated using the elastic constant.[54] The mechanical properties of the metals employed in a material determine the variety of uses for that material and the length of anticipated service life.[55] Based on the imposed strain, we calculated the elastic coefficients C_{11}, C_{12}, and C_{44}. C_{11} and C_{12} show how longitudinal elasticity properties change as the stress differs. In addition, the rest constant C_{44}, frequently used to relate the mechanical rigidity and crystal form deformation,[56] is used to observe the variations in shape elasticity. The connection between Cauchy pressure as well as material ductility is created by the angular shape of atomic bonds in metals.[57] A crystal is considered to be ductile or brittle depending on whether its Cauchy pressure is positive or negative.[58] The outcomes of this DFT calculation of the elastic constants for Ca_3AsBr_3 are shown in Figure 4a, and the elastic moduli are shown in Figure 4b. Furthermore, because the stress applied altered the lattice constant, it is critical to understand how the mechanical properties will change. The material may also be categorized and characterized according to its mechanical characteristics. Figure 5b shows that the Cauchy pressure rises as the stress does and maintains a positive value across the range of recorded pressure levels. This demonstrates the substantial degree of ductility shown by the Ca_3AsBr_3 material. The Pugh's ratio after applying stress is shown in Figure 5a. The material has grown more ductile due to increased applied stress, which has also increased the mechanical stability. The renowned Born stability criteria,[59] as presented below, explain the mechanical stability of Ca_3AsBr_3 adequately: $C_{11} > 0$, $C_{44} > 0$, $C_{11} + 2C_{12} > 0$, C_{11}-$C_{12} > 0$.

According to the findings, the Ca_3AsBr_3 metal halide is mechanically stable to a wide range of pressure fluctuations

https://doi.org/10.1021/acsomega.3c08131
ACS Omega 2024, 9, 8005−8018

Table 1. Minimum, Maximum Values of the Young'S Modulus, Compressibility, Shear Modulus, Poisson'S Ratio and the Ratio *A* of Ca_3AsBr_3

Pressure (GPa)	Y_{min} (GPa)	Y_{max} (GPa)	A_Y	K_{min} (TPa^{-1})	K_{max} (TPa^{-1})	A_K	G_{min} (GPa)	G_{max} (GPa)	A_G	ν_{min}	ν_{max}	A_ν
0	45.43	75.96	1.67	9.57	9.57	1.00	17.71	33.425	1.89	0.09	0.43	4.70
50	26.57	480.94	18.1	1.68	1.68	1.00	8.99	219.61	24.43	0.01	0.93	136.05

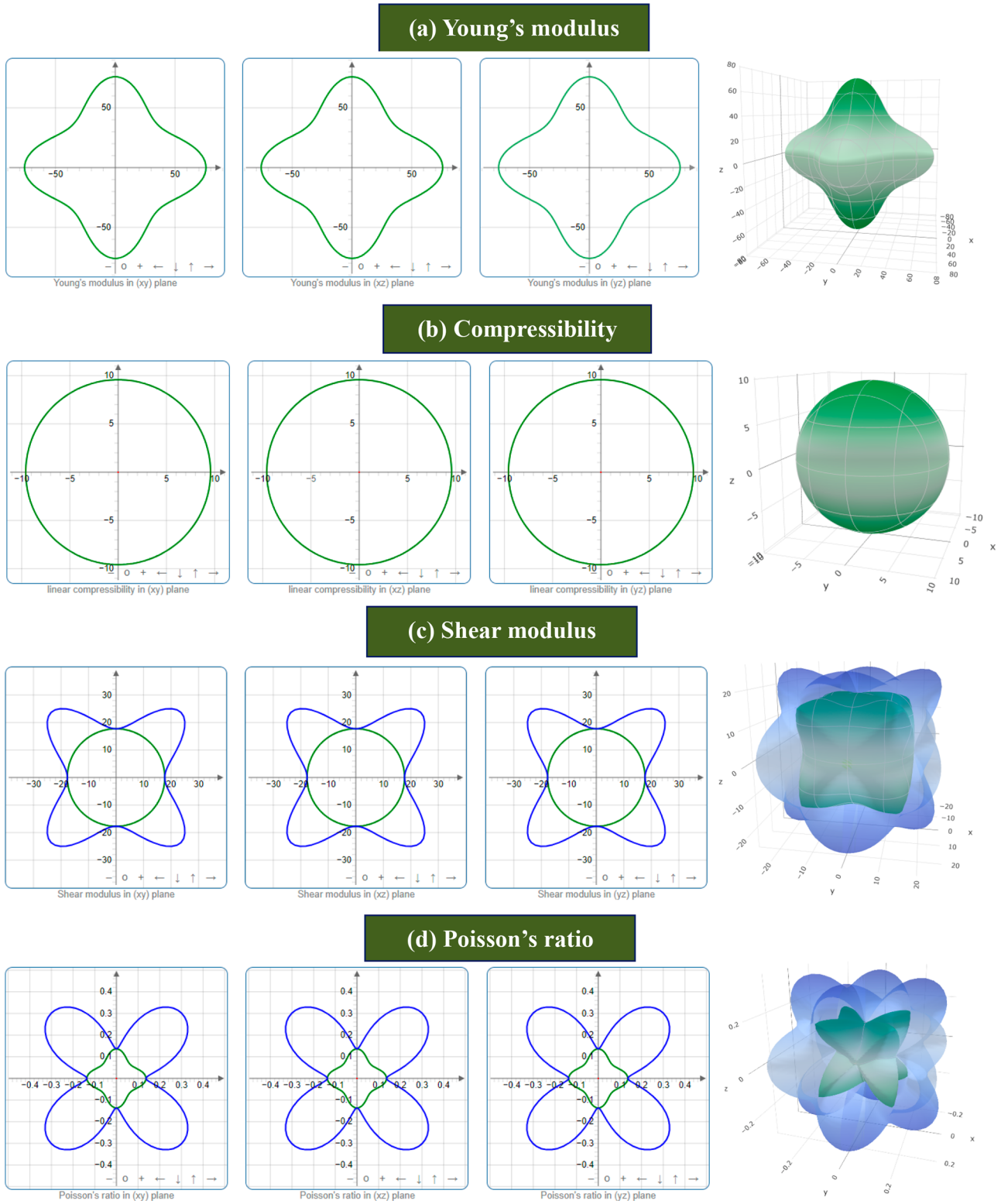

Figure 6. 2D and 3D plots of (a) *Y*, (b) *K*, (c) *G*, and (d) ν of Ca_3AsBr_3 at 0 GPa.

https://doi.org/10.1021/acsomega.3c08131
ACS Omega 2024, 9, 8005−8018

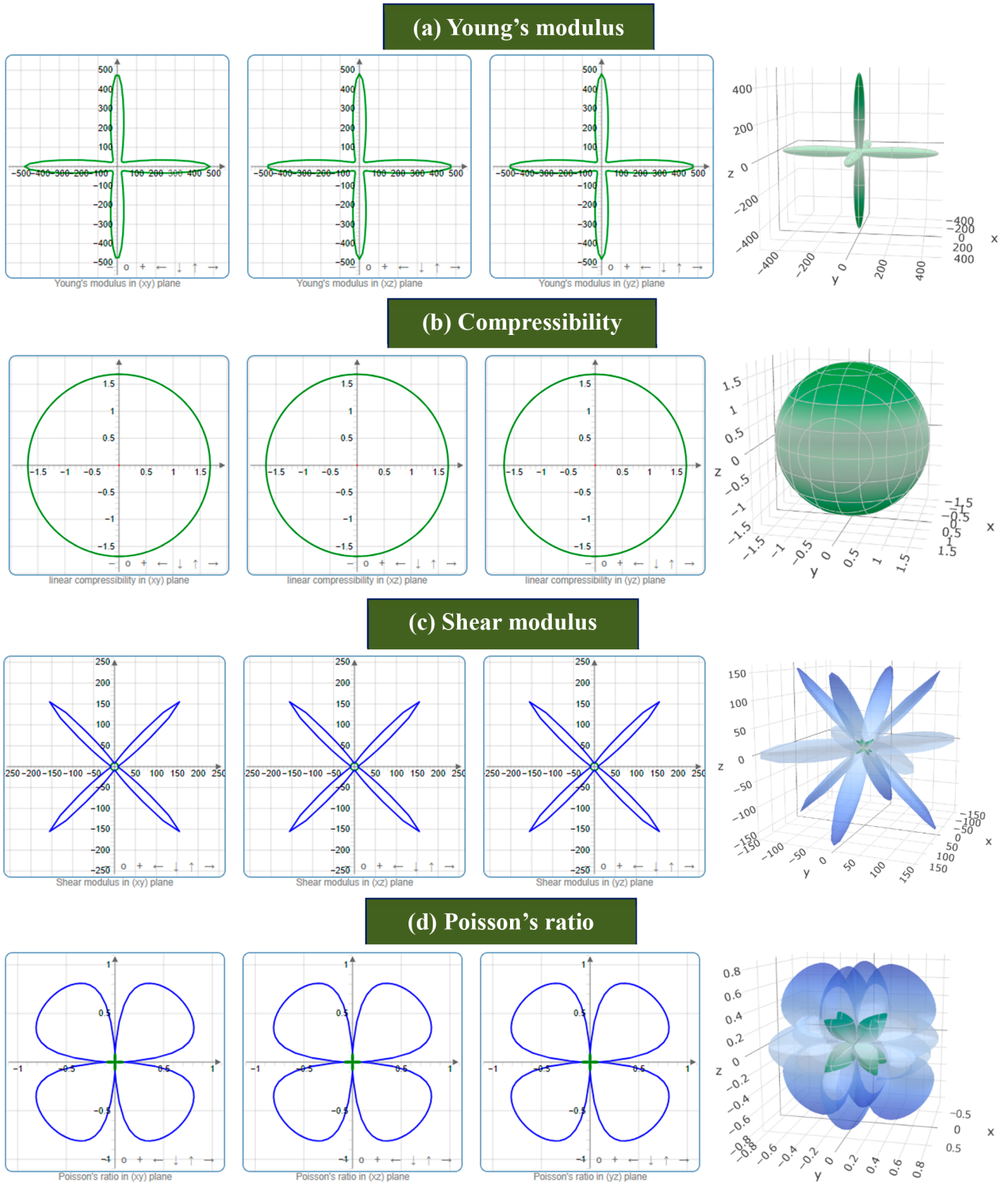

Figure 7. 2D and 3D plots of (a) *Y*, (b) *K*, (c) *G*, and (d) ν of Ca_3AsBr_3 at 50 GPa.

and fulfills the Born stability requirements. Furthermore, it is clear that the values of C_{11}, C_{12}, and C_{44} rise when the outer hypostatic pressure is added. Among the essential mechanical parameters are the bulk modulus (shown by *B*), shear modulus (shown by *G*), Young's modulus (shown by *E*), Pugh's ratio (shown by *B*/*G*), and Poisson's ratio (shown by *n*). A material's overall modulus is a measure of its rigidity as well as flexibility. The shear modulus may determine how much a material can deform plastically in reaction to pressure. The rise in the modulus of bulk, shear, and Young's modulus along with pressure is observed because pressure increases the intermolecular or interatomic forces in the Ca_3AsBr_3 compound. This makes it more robust against volume changes, shear deformation as well as deformation in the axial direction.

https://doi.org/10.1021/acsomega.3c08131
ACS Omega 2024, 9, 8005−8018

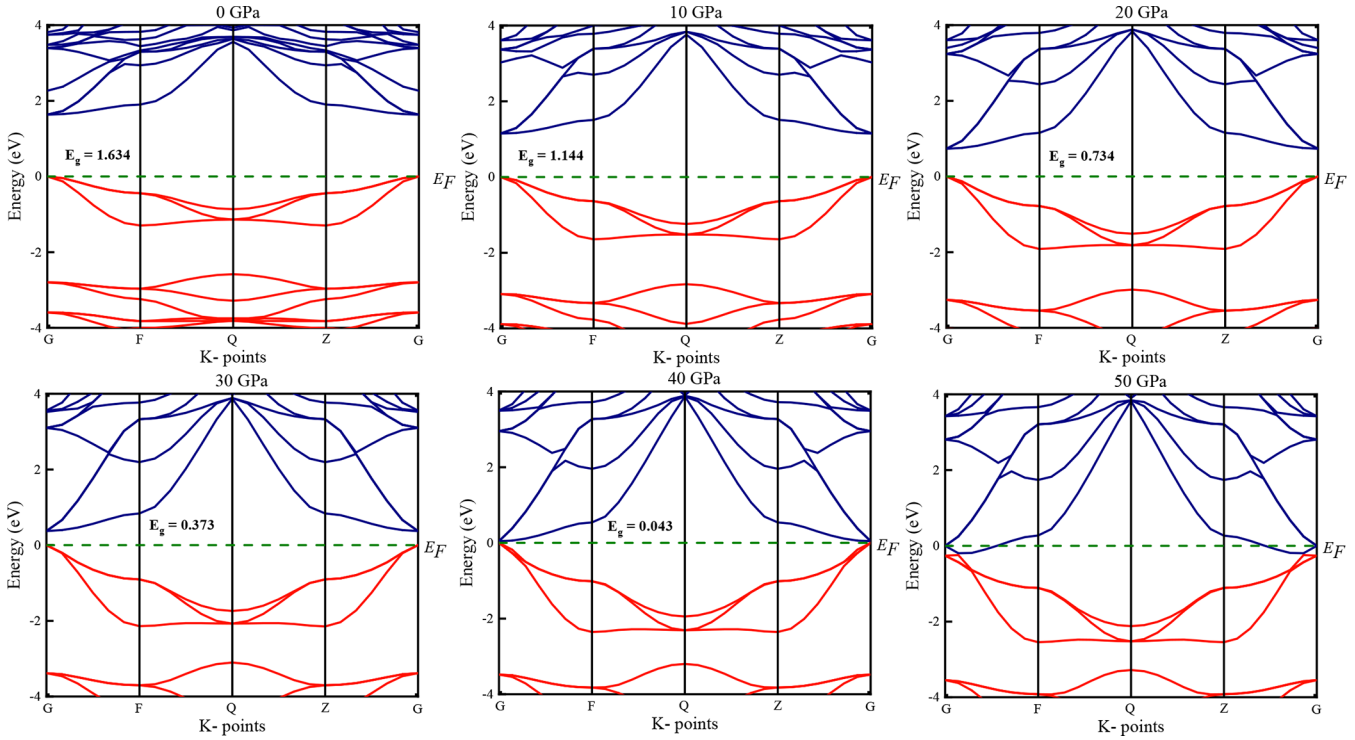

Figure 8. Electronic band structure of Ca_3AsBr_3 under pressure and the band gap shrink with the increase of pressure.

Pugh's ratio is another name for the bulk modulus to shear modulus ratio (B/G).[60] The mechanical properties of a material, such as brittleness and ductility, are related to Poisson's and Pugh's ratios.[55] In general, the Pugh's and Poisson ratios, which distinguish between ductile and brittle substances, are considered as critical values of 1.75 and 0.26, respectively.[61] Calculated and presented ratios such as the Poisson's and Pugh's ratios demonstrate a greater degree of ductility. Initially, these materials exhibit brittle behavior (about 0 GPa), but with increased pressure within the range mentioned, they become more ductile.[62] The minimum and maximum values of Young's modulus, compressibility, shear modulus, Poisson's ratio, and the ratio A of Ca3AsBr3 are listed in Table 1.

Therefore, it can be claimed that this material is particularly beneficial for creating devices and real-world applications. The 3D visual illustrations of the direction dependence of Young's modulus (E), shear modulus (G), and Poisson's ratio (ν) at 0 GPa pressure were demonstrated using the ELATE tool[63] and are shown in Figure 6a−d, respectively, to further explain the anisotropic nature.[64,65] Figure 7a−d show the same phenomenon at 50 GPa. The circular 2D and 3D plots show complete isotropy, and their aberrations represent a material's anisotropy. The 3D graphs show that the compounds examined are anisotropic in all directions. There is, however, a greater spherical 3D deviation when the pressure is 50 GPa than when it is 0 GPa, indicating that the greater the pressure, the greater the anisotropy.

3.3. Electronic Properties. The electrical band structures of two different unstressed (0 GPa) and stressed (10 to 50 GPa) materials were calculated to better understand the unique electronic properties of Ca_3AsBr_3. The electronic band configuration of Ca_3AsBr_3 is determined by the highly arranged symmetric Brillouin zone positions (G, F, Q, Z, and G), and the overall structure displays the band architecture recurring through these points. The high-symmetry k-path to the initial Brillouin zone is shown in Figure 8. The Fermi energy level remained constant at nil to make it simple to determine the bandgap value from the graphic. According to Figure 8, the G-point is where the conduction band's minimum (CBM) as well as the valence band's maximum (VBM) are found. It may be inferred from this that the Ca_3AsBr_3 material under study has a direct bandgap structure, corresponding to a bandgap value of around 1.63 eV when applying the PBE functional. Over the whole stressed engineering process, Ca_3AsBr_3 retained its direct bandgap electrical structure. When the stress was changed between 0 and 50 GPa, the Ca_3AsBr_3's bandgaps were tuned from 1.63 to 0 eV. In particular, different bandgap values were observed at different stress levels, such as 0 GPa (1.634 eV), 10 GPa (1.144 eV), 20 GPa (0.734 eV), 30 GPa (0.373 eV), 40 GPa (0.043 eV), and 50 GPa (0 eV). An optimal bandgap of 1.14 eV can be achieved by tuning Ca_3AsBr_3 under 10 GPa stress conditions. Polman et al. showed the optimal semiconductor bandgap of 1.34 eV was instrumental to achieving the highest efficiency of photovoltaic energy conversion in single-junction solar cells.[66] Our optimal band gap is close to that value. Pressure affects the transition from a semiconductor to a metallic state. The bandgap was undervalued when it was evaluated using the GGA approach. The GGA approach often runs into issues like these. Additionally, the LDA+ U[67] (local density approximation) approaches showed an underestimation of the bandgap. Some researchers have suggested the GW method[68] and hybrid functional[69] as two methods to get around this kind of bandgap computation. Each of these methods has a unique set of limitations, however. The hybrid potential proposed by HSE[70] may raise the simulated bandgap values to within a small range of the empirically determined value, albeit this is not always the case. Additionally, the ideal value may undergo certain modifications using the GGA+U[71] approach. This

https://doi.org/10.1021/acsomega.3c08131
ACS Omega 2024, 9, 8005−8018

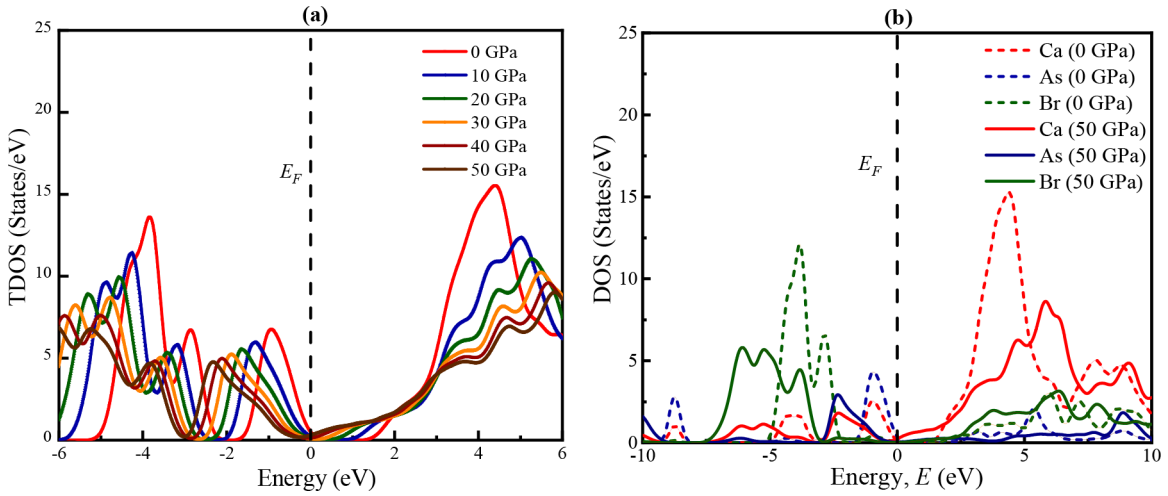

Figure 9. Calculated (a) TDOS of the Ca_3AsBr_3 compound at 0, 10, 20, 30, 40, and 50 GPa and (b) DOS of Ca, As and Br atoms in the Ca_3AsBr_3 compound at 0 and 50 GPa pressure.

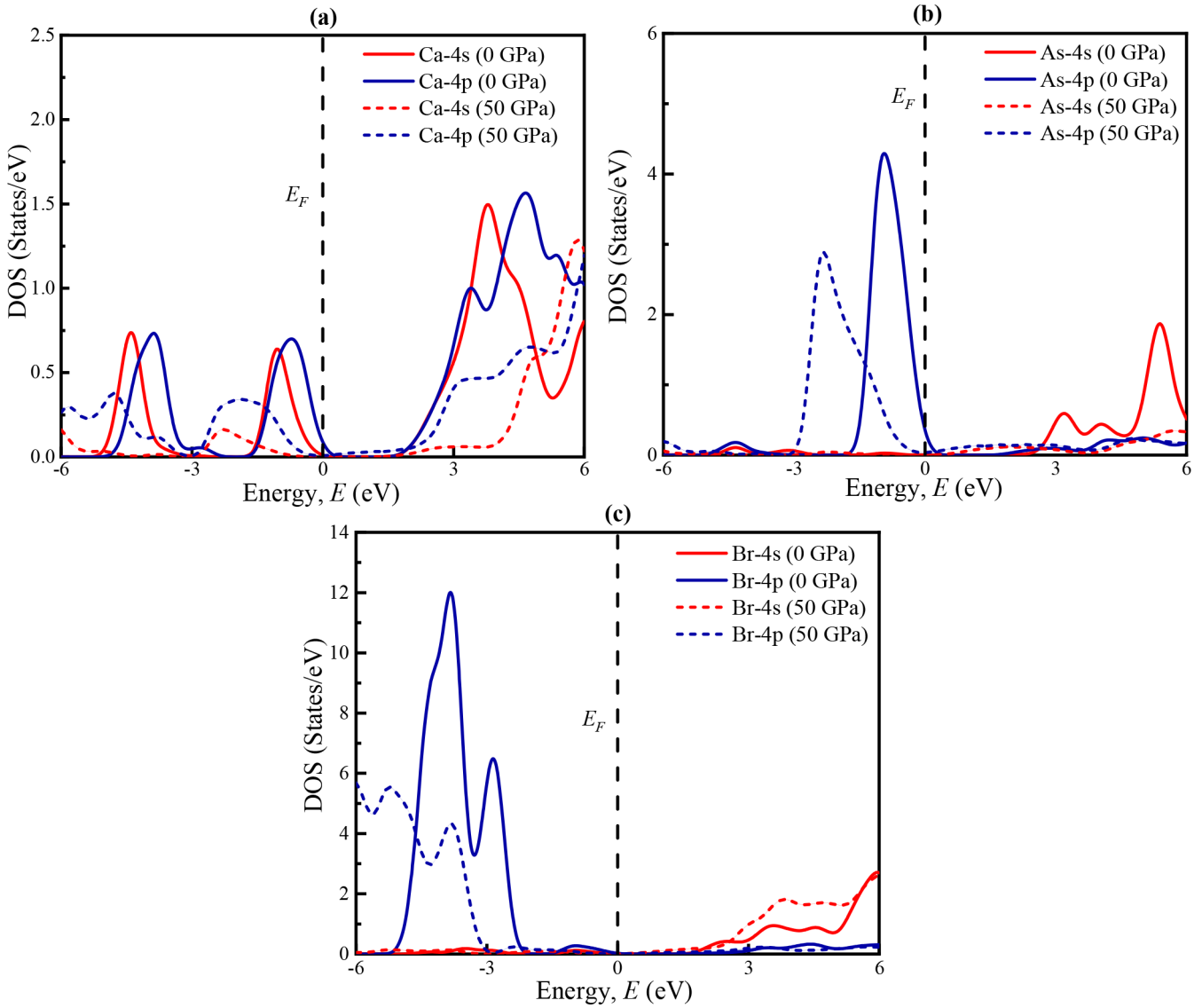

Figure 10. Calculated PDOS of (a) Ca, (b) As, and (c) Br of Ca_3AsBr_3 at 0 and 50 GPa pressure.

https://doi.org/10.1021/acsomega.3c08131
ACS Omega 2024, 9, 8005−8018

Table 2. Mulliken Atomic Populations of Ca_3AsBr_3

Compound	P (GPa)	Species	s	p	d	Total	Charge	Bond	Population	Length (Å)
Ca_3AsBr_3	0	Ca	2.43	6.64	0.66	9.73	0.27	Ca−As	0.96	2.98
		As	1.59	4.03	0.00	5.62	−0.62			
		Br	1.61	5.45	0.00	7.06	−0.06	Ca−Br	0.11	2.98
	50	Ca	2.25	6.50	1.20	9.94	0.06	Ca−As	0.55	2.51
		As	1.67	3.84	0.00	5.51	−0.51			
		Br	1.60	5.29	0.00	6.89	0.11	Ca−Br	0.29	2.51

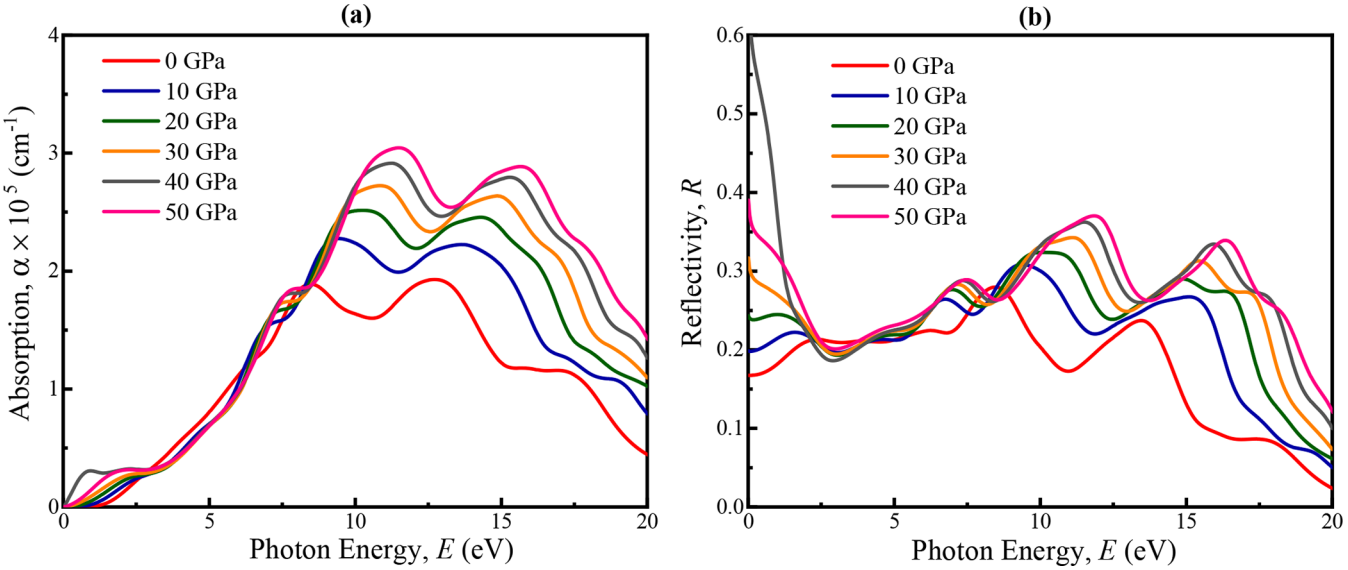

Figure 11. Optical functions of (a) absorption and (b) reflectivity of Ca_3AsBr_3 under different pressures.

study, however, ignored the bandgap inaccuracy introduced by the GGA approach in favor of focusing just on the effect of stress on the bandgap of Ca_3AsBr_3 Depending on the specific material and application requirements, direct or indirect band gaps are potentially suitable for solar, photothermal, or optoelectronic devices. Simulated Ca_3AsBr_3's direct bandgap value suggests it is the best material for optoelectronic applications. The Ca_3AsBr_3 band topologies that result from hypostatic stress between 0 and 50 GPa are shown in Figure 9 as a function of the density of states. The total density of states (TDOS) gives us the idea of hybridization, band intersecting phenomenon and bond formation. We examined the effects of stresses ranging from 0 to 50 GPa (with an interval of 10 GPa in each direction) on the Ca_3AsBr_3 structures. The partial density of states (PDOS), which depicts the influence of individual atoms and their many states, is often used to determine the bandgap energy of Ca_3AsBr_3 formations. PDOS provides an illustration of the energetic level of an orbit on its density of states. The quantity known as the density of state, or DOS for short, is obtained by adding up all of the projections. The variation of PDOS measurements for Ca_3AsBr_3 crystals across the energetic range of −6 to +6 eV is shown in Figure 10. The contribution of the orbital Ca, As, and Br atoms is likewise altered by stress. The PDOS of Ca_3AsBr_3 as a function of energy. As the stress changes from 0 to 50 GPa, the PDOS filled by the 4p orbital of Br atoms shows a presence toward the valence band side, below the Fermi level. The 4p orbital in the conduction band area dominates the total DOS of the Ca atoms. The static position and structure of the occupied DOS of the Ca's 4p orbital in the conduction band are affected by changes in stress. As a result, the total DOS contribution is decreasing. As can be observed in the figure, the Ca_3AsBr_3 structure's total DOS decreases from around 15 electrons/eV (at 0 GPa) to about 10 electrons/eV (at 50 GPa). The conjugated hybridized Ca−Br and As−Br orbitals are seen beyond the bandgap in all of the energy rangesCa_3AsBr_3's hybridized Ca and as states with Br cover the whole energy spectrum while avoiding the bandgap. The Ca−Br as well as As−Br bonds are examples of covalent bonds. In the substance Ca_3AsBr_3, the charge shifts from Ca and As to Br as a result of the extreme differences in atomic states. Ca^{2+} atoms have a minimal impact close to the Fermi level. When we studied Ca_3AsBr_3 in its cubic stage, we discovered that the As-p orbital and the Ca-p orbitals individually contributed just a little to the band of conduction. In contrast, the Br-p orbital was predominant over each of the two in the band of valence.

Mulliken charge analysis is computed, and it is shown in Table 2. Based on Table 2, As and Br have negative charges in the Ca_3AsBr_3 material, which indicates that positive charges from Ca atoms can be transferred into As and Br. The Ca−As bond in Ca_3AsBr_3, has a value of 0.96, indicating that 96% of the electrons are shared by the two molecules. This suggests that the Ca−As bond could be an exceptionally solid bond. The Ca−Br bond population of 0.11 implies that 11% of the electrons are shared between the two atoms in the Ca−Br bond. This demonstrates that compared to the Ca−As bond, the Ca−Br bond is substantially weaker. The difference in electronegativity between the two atoms is what causes the difference in bond populations between the Ca−As and Ca−Br bonds. Arsenic is more electronegative than bromine, meaning that it has a stronger attraction for electrons, resulting in a stronger bond between the calcium and arsenic atoms. The

https://doi.org/10.1021/acsomega.3c08131
ACS Omega 2024, 9, 8005−8018

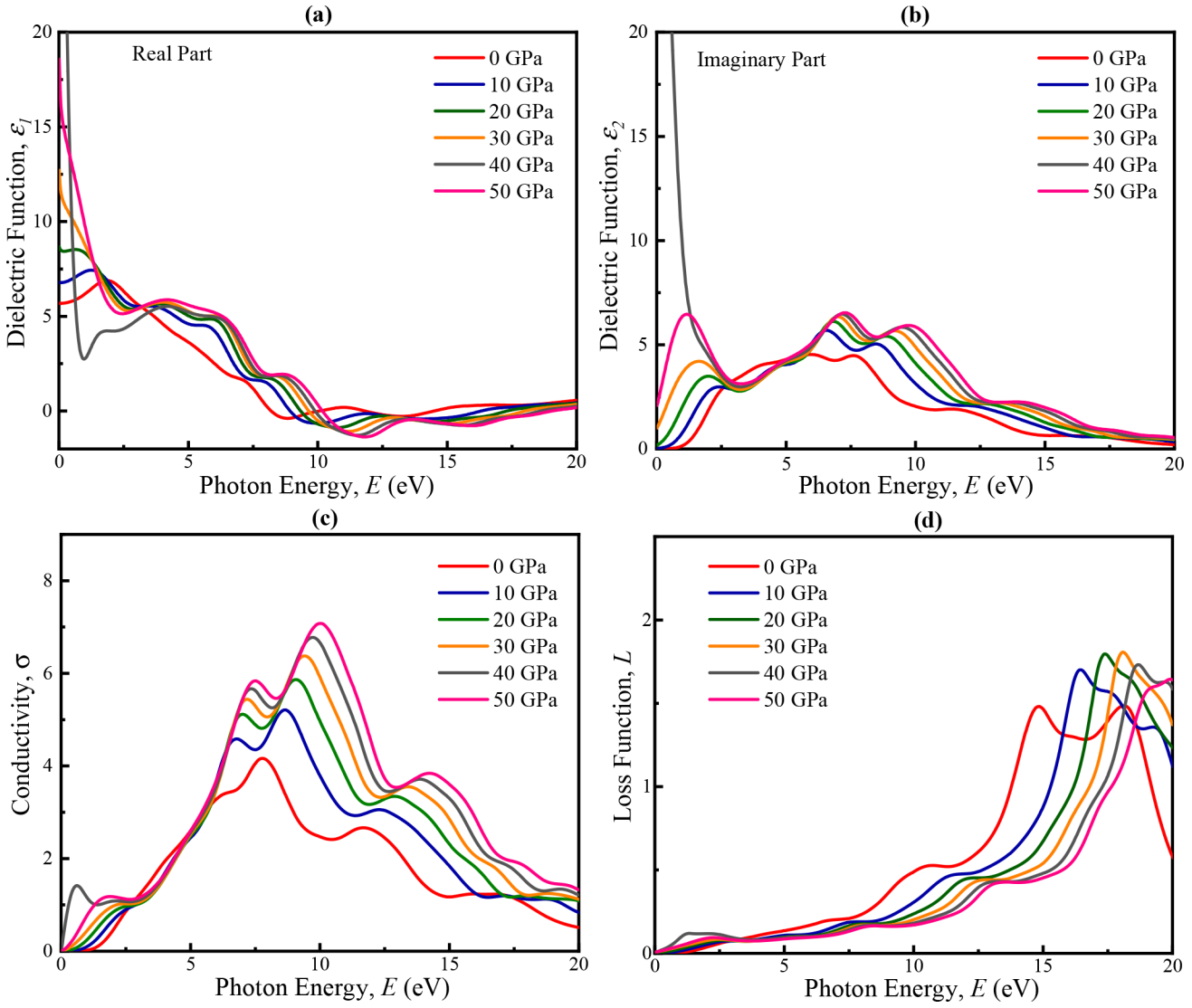

Figure 12. Different pressures of the optical properties of (a) the real part of the dielectric function, (b) the imaginary part of the dielectric function, (c) the conductivity, and (d) the loss function of Ca_3AsBr_3.

compression of the material, which influences the bonding interactions between atoms and molecules, results in a reduction in bond population and bond length under applied pressure. The Ca_3AsBr_3 VBM and CBM moved toward the Fermi energy level during hypostatic stress (0 to 50 GPa). However, the CBM and VBM both remained at the G-point. The bond length between the Ca, As, and Br was decreased as a consequence of the orbital overlapping that developed as a result of imposing stress. The pressure caused a straight bandgap to appear at the G-point. The bandgap was shown to narrow with more significant stress for every single specimen, as seen in Figure 8. Nevertheless, the electric band structure changed when the stress grew from 0 to 50 GPa, as shown in Figure 8. As the stresses increased, the VBM and CBM shifted further from the Fermi level, widening the bandgap. Due to the hypostatic pressure, the repulsion force between the Ca, As, and Br atoms reduced as their bond lengths became smaller and their atomic distance decreased.

3.4. Optical Properties. It is possible to determine a material's suitability for optoelectronic applications by looking at its optical characteristics, which include measurements of the absorption, reflectivity, dielectric functions, conductivity, and loss function.[32] Hydrostatic stress is a thermomechanical method that may improve a material's visible properties by altering the lattice parameter.[72−75] The distance that light of a given wavelength traverses before it is absorbed may be calculated by examining the coefficients of absorption whenever light strikes the outermost layer of a material. It is also conceivable to specify the ideal solar energy conversion effectiveness range, and this is essential for use in applications involving photovoltaics. In this study, it was discovered that Ca_3AsBr_3's optical properties can be tuned across a pressure range of 0 to 50 GPa. The photon-energy-intensive coefficients of absorption for the stressed Ca_3AsBr_3 structures are shown in Figure 11a. Because it shows the largest wavelength that a material can absorb, the first absorption peak appears to be the most important in photovoltaic applications.[76,77] Because photovoltaics employ this information, it is significant. Ca_3AsBr_3 had very poor absorption characteristics in the near-visible region of the optical spectrum in the absence of any external stress, as seen in Figure 11a. Compared to the initial conditions, the absorption edge of Ca_3AsBr_3 under stress migrated to the higher energy area. In contrast, Ca_3AsBr_3 under hydrostatic stress went into the low energy region,

https://doi.org/10.1021/acsomega.3c08131
ACS Omega 2024, 9, 8005−8018

proving a red shift. Hypostatic stress causes a significant rise in the Ca_3AsBr_3 absorption spectra in the visible and UV regions. Stressed Ca_3AsBr_3 exhibits a larger range of light absorption than their nonstressed counterparts, making them a desirable candidate for use in photovoltaics. Due to the fact that Ca_3AsBr_3's absorption maxima moves toward the UV region under stress, it is an excellent candidate for use in the creation of medical equipment disinfection devices. In Figure 11b, the reflectivity of the substance is demonstrated, which is opposite to the absorption phenomenon but indicating the same applications. Materials having absorbance maxima between 11 to 17 eV show proficiency with applications for ultraviolet light. Figure 11b shows the high reflectivity of at low photon energies because most of the photons incident on the surface are being reflected and relatively few are being absorbed. The reflectivity of Ca_3AsBr_3 decreases with increasing photon energy. The Ca_3AsBr_3 material absorbs more photons when under higher pressures, so the reflectivity decreases more slowly. Ca_3AsBr_3 is also suitable for a wide range of other applications such as optical storage and solar energy conversion.

In the remainder of the formula of the dielectric function $\varepsilon(\omega)$, both real and imaginary components are indicated by the symbols $\varepsilon_1(\omega)$ and $\varepsilon_2(\omega)$ as follows:

$$\varepsilon(\omega) = \varepsilon_1(\omega) + i\varepsilon_2(\omega) \tag{1}$$

The real dielectric function was obtained via the Kramers–Kronig transformation.[78] The components of the momentum matrix corresponding to the hypothetical dielectric function were also taken into consideration.[79] Figure 12a shows the dielectric constants for the stressed real portion for photon energy up to 20 eV. The real component data of the constant of dielectric might be used to calculate the impact of polarization as well as dispersion. The symbol $\varepsilon_1(0)$, which stands for frequency limits to zero and is a subset of the real component $\varepsilon_1(0)$, denotes an essential parameter for the investigation of optical phenomena. At a pressure of 0 GPa, the value of $\varepsilon_1(0)$, for cubic Ca_3AsBr_3 was discovered to be 5.5. The increase in the value of $\varepsilon_1(0)$, from its starting value of $\varepsilon_1(0)$, following exposure to optical radiation is proof that the material has a strong capacity for light spectrum absorption in the visible region. The positive values of $\varepsilon_1(\omega)$ pointed to the greatly increased refractive index and semiconducting characteristics of unstressed Ca_3AsBr_3. The peak dielectric constant of the Ca_3AsBr_3 material crystals were changed by varying the hydrostatic pressure. Because the band gap narrowed and shifted to a lower wavelength with increasing stress, Ca_3AsBr_3 had a greater stationary dielectric constant under all stresses.

The hydrostatic pressure also resulted in the first peak exhibiting a red-shift inside the visible area and a diminishing pattern consistent with stress-dependent band structure expectations. At 50 GPa, the actual portion of the dielectric function was measured to be around 18. Ca_3AsBr_3 could be used as a nanocoating material that operates in the infrared spectrum because of its characteristics. For high-band gap elements compared to low-band gap substances, the dielectric constant peaks are lower. The Ca_3AsBr_3 structures displayed greater dielectric constant peaks and a red shift to greater wavelengths of photon energies since the band gap shrank with increased hydrostatic stress. Figure 12b shows the behavior of the imaginary dielectric constant, $\varepsilon_2(\omega)$, under stress. The imaginary dielectric function $\varepsilon_2(\omega)$ may be used to predict interband transition energies close to the Fermi level and the characteristics of the materials' spectrum absorption. Ca_3AsBr_3's $\varepsilon_2(\omega)$ values predominated the absorbance spectrum. It demonstrates how, when stress is applied, the imaginary component of the dielectric function expands and goes to the high wavelength region. The transition of the particles from valence to conduction bands relies on these hypothetical absorption peaks. Because of changes made to the lattice parameter and bandgap, the peak locations have been shifted. When hydrostatic stress is applied, the imaginary points show a redshift at the lower energy region and a blueshift at the higher energy region, correspondingly. This indicates that the hydrostatic stress may alter the absorption spectrum range of the Ca_3AsBr_3 material under study.

A substance's photon conductance is referred to as photoconductivity.[33] It offers the ability to conduct electricity in the presence of different fields of electromagnetic radiation. The spectral conductivity of Ca_3AsBr_3 is demonstrated in Figure 12c. With an increased pressure, the conductivity increases. In the presence of high pressure, the material exhibits a significant increase in the absorption spectra and optical conductivity, demonstrating the possibility of utilizing it as a solar cell. The loss function is another property that measures the energy driven away by an electron as it moves in an insulator. It is symbolized by $L(\omega)$.

$$L(\omega) = \mathcal{T}\left(\frac{-1}{\varepsilon(\omega)}\right)$$

or in labels of $\varepsilon_1(\omega)$ and $\varepsilon_2(\omega)$,

$$L(\omega) = \frac{\varepsilon_2(\omega)}{\varepsilon_1^2(\omega) + \varepsilon_2^2(\omega)} \tag{2}$$

In Figure 12d, we observe the loss function of Ca_3AsBr_3 under unstressed conditions. Peaks in the diagrams of loss function uncovered that photon energy was mislaid when the upcoming photon energy was more significant than the substance's bandgap for the Ca_3AsBr_3 compounds. For the universal cubic structure of Ca_3AsBr_3, the $L(\omega)$ peaks emerged across 13 to 18 eV. Figure 8 proved that underneath the bandgap, no dispersion was observed. Several notorious peaks were in the ultraviolet province of the loss function diagram, demonstrating that this province was where the mainstream of electron loss and resonance occurred for the Ca_3AsBr_3 monolayer. Since the energy loss function stages were not noticeably present below 1 eV, it was transparent that Ca_3AsBr_3 would be an efficient absorber in the visible light and near-IR region.

4. CONCLUSION

Finally, using the first-principles DFT theory, we thoroughly explored the structural, mechanical, and optoelectronic characteristics of the inorganic material Ca_3AsBr_3. The Ca_3AsBr_3 substances showed a red shifting phenomenon in the visible region and its increasing absorption and optical conductivity peaks after applying hydrostatic pressure. At 50 GPa pressure, semiconductor to metallic transition opens some door to applications in the optoelectronic arena where metallic system is a prerequisite. Also X-ray diffraction data confirms cubic cell retention even after applying pressure/stress uniformly from all directions. The distribution of density states demonstrates that As and Br atom orbitals provide the greatest contribution to VBM and CVB, with Ca atoms making the smallest contributions. Ca_3AsBr_3 compounds may be used for photovoltaic purposes because of their high ductility as well

https://doi.org/10.1021/acsomega.3c08131
ACS Omega 2024, 9, 8005−8018

as mechanical stability, as demonstrated by their stress-induced mechanical characteristics. By adjusting the band configuration, dielectric coefficient, and elastic constant quantities via stress variation, Ca_3AsBr_3's physical and structural rigidity may be maintained while its potential for large photon absorption is increased. Our findings point to the potential for Ca_3AsBr_3 to become a dominant material for usage in optical systems, and we expect to see this happen soon.

■ ASSOCIATED CONTENT

Supporting Information

The Supporting Information is available free of charge at https://pubs.acs.org/doi/10.1021/acsomega.3c08131.

The computed and available theoretical lattice constants and evaluated unit cell volume of Ca_3AsBr_3 at various pressures; the elastic constants and Cauchy pressure values for cubic Ca_3AsBr_3 perovskites at varying pressures, which aid in understanding their mechanical behavior and performance; the detailed information on the mechanical properties of Ca_3AsBr_3, which can be used to assess the material's suitability for a variety of applications and to inform future research (PDF)

■ AUTHOR INFORMATION

Corresponding Author

Md. Arif Ul Islam − *Department of Physics, University of Barishal, Barishal 8200, Bangladesh; Department of Electrical and Mechanical Engineering, Nagoya Institute of Technology, Showa-Ku, Nagoya 466-8555, Japan;* orcid.org/0000-0002-6857-4727; Email: m.islam.622@stn.nitech.ac.jp

Authors

Ovijit Das − *Department of Materials Science and Engineering, University of Connecticut, Storrs, Connecticut 06269, United States*

Dev Bahadur Khadka − *Department of Electrical and Mechanical Engineering, Nagoya Institute of Technology, Showa-Ku, Nagoya 466-8555, Japan*

Md. Rasidul Islam − *Department of Electrical and Electronic Engineering, Bangamata Sheikh Fojilatunnesa Mujib Science and Technology University, Jamalpur 2012, Bangladesh;* orcid.org/0000-0002-9916-793X

Md. Ferdous Rahman − *Advanced Energy Materials and Solar Cell Research Laboratory, Department of Electrical and Electronic Engineering, Begum Rokeya University, Rangpur 5400, Bangladesh;* orcid.org/0000-0002-0090-2384

Shinya Kato − *Department of Electrical and Mechanical Engineering, Nagoya Institute of Technology, Showa-Ku, Nagoya 466-8555, Japan*

Tetsuo Soga − *Department of Electrical and Mechanical Engineering, Nagoya Institute of Technology, Showa-Ku, Nagoya 466-8555, Japan*

Complete contact information is available at: https://pubs.acs.org/10.1021/acsomega.3c08131

Notes

The authors declare no competing financial interest.

■ REFERENCES

(1) Islam, M. A.; Kato, S.; Kishi, N.; Soga, T. Enhanced Surface Morphology and Photovoltaic Properties of a New Class of Material Copper Silver Bismuth Iodide Solar Cell. *Journal of Materials Research and Technology* **2023**, *25*, 4171−4186.

(2) Zheng, W.; Wang, X.; Zhang, X.; Chen, B.; Suo, H.; Xing, Z.; Wang, Y.; Wei, H.-L.; Chen, J.; Guo, Y.; Wang, F. Emerging Halide Perovskite Ferroelectrics. *Adv. Mater.* **2023**, *35* (21), 2205410.

(3) Green, M. A.; Ho-Baillie, A.; Snaith, H. J. The Emergence of Perovskite Solar Cells. *Nat. Photonics* **2014**, *8* (7), 506−514.

(4) Correa-Baena, J.-P.; Saliba, M.; Buonassisi, T.; Grätzel, M.; Abate, A.; Tress, W.; Hagfeldt, A. Promises and Challenges of Perovskite Solar Cells. *Science* **2017**, *358* (6364), 739−744.

(5) Jung, H. S.; Park, N. Perovskite Solar Cells: From Materials to Devices. *small* **2015**, *11* (1), 10−25.

(6) Kim, J. Y.; Lee, J.-W.; Jung, H. S.; Shin, H.; Park, N.-G. High-Efficiency Perovskite Solar Cells. *Chem. Rev.* **2020**, *120* (15), 7867−7918.

(7) Pacchioni, G. Highly Efficient Perovskite LEDs. *Nat. Rev. Mater.* **2021**, *6* (2), 108.

(8) Zhang, K.; Zhu, N.; Zhang, M.; Wang, L.; Xing, J. Opportunities and Challenges in Perovskite LED Commercialization. *Journal of Materials Chemistry C* **2021**, *9* (11), 3795−3799.

(9) Mitzi, D. B. Templating and Structural Engineering in Organic-Inorganic Perovskites. *J. Chem. Soc., Dalton Trans.* **2001**, No. 1, 1−12.

(10) Mitzi, D. B.; Chondroudis, K.; Kagan, C. R. Organic-Inorganic Electronics. *IBM J. Res. Dev.* **2001**, *45* (1), 29−45.

(11) Mitzi, D. B. Thin-Film Deposition of Organic- Inorganic Hybrid Materials. *Chem. Mater.* **2001**, *13* (10), 3283−3298.

(12) Tan, Z.-K.; Moghaddam, R. S.; Lai, M. L.; Docampo, P.; Higler, R.; Deschler, F.; Price, M.; Sadhanala, A.; Pazos, L. M.; Credgington, D.; et al. Bright light-emitting diodes based on organometal halide perovskite. *Nat. Nanotechnol.* **2014**, *9*, 687−692.

(13) Das, O.; Saiduzzaman, M.; Hossain, K. M.; Shuvo, I. K.; Rahman, M. M.; Ahmad, S.; Mitro, S. K. First-Principles Calculations to Investigate Pressure-Driven Electronic Phase Transition of Lead-Free Halide Perovskites KMCl3 (M = Ge, Sn) for Superior Optoelectronic Performance. *Results in Physics* **2023**, *44*, 106212.

(14) Kojima, A.; Teshima, K.; Shirai, Y.; Miyasaka, T. Organometal Halide Perovskites as Visible-Light Sensitizers for Photovoltaic Cells. *J. Am. Chem. Soc.* **2009**, *131* (17), 6050−6051.

(15) Jiang, Q.; Zhao, Y.; Zhang, X.; Yang, X.; Chen, Y.; Chu, Z.; Ye, Q.; Li, X.; Yin, Z.; You, J. Surface Passivation of Perovskite Film for Efficient Solar Cells. *Nat. Photonics* **2019**, *13* (7), 460−466.

(16) Ali, A. H.; Ahmed, A. M.; Abdel-Khaliek, A. A.; Abd El Khalik, S.; Abass, S. M.; Shaban, M.; Rabia, M. Preparation of Inorganic Lead-Free CuO/Cs2SnCl6-KI Perovskite for Green Hydrogen Production from Wastewater by Using Solar Energy. *J. Photochem. Photobiol., A* **2023**, *445*, 115102.

(17) Liu, J.; Li, N.; Jia, J.; Dong, J.; Qiu, Z.; Iqbal, S.; Cao, B. Perovskite Films Grown with Green Mixed Anti-Solvent for Highly Efficient Solar Cells with Enhanced Stability. *Sol. Energy* **2019**, *181*, 285−292.

(18) Tian, S.; Li, J.; Li, S.; Bu, T.; Mo, Y.; Wang, S.; Li, W.; Huang, F. A Facile Green Solvent Engineering for Up-Scaling Perovskite Solar Cell Modules. *Sol. Energy* **2019**, *183*, 386−391.

(19) Dandia, A.; Saini, P.; Sharma, R.; Parewa, V. Visible Light Driven Perovskite-Based Photocatalysts: A New Candidate for Green Organic Synthesis by Photochemical Protocol. *Current Research in Green and Sustainable Chemistry* **2020**, *3*, 100031.

(20) Rolston, N.; Bush, K. A.; Printz, A. D.; Gold-Parker, A.; Ding, Y.; Toney, M. F.; McGehee, M. D.; Dauskardt, R. H. Engineering Stress in Perovskite Solar Cells to Improve Stability. *Adv. Energy Mater.* **2018**, *8* (29), 1802139.

(21) Liu, D.; Luo, D.; Iqbal, A. N.; Orr, K. W. P.; Doherty, T. A. S.; Lu, Z.-H.; Stranks, S. D.; Zhang, W. Strain Analysis and Engineering in Halide Perovskite Photovoltaics. *Nature materials* **2021**, *20* (10), 1337−1346.

(22) Zhan, Y.; Cheng, Q.; Song, Y.; Li, M. Micro-Nano Structure Functionalized Perovskite Optoelectronics: From Structure Functionalities to Device Applications. *Adv. Funct. Mater.* **2022**, *32* (24), 2200385.

(23) Liu, Y.; Kim, D.; Ievlev, A. V.; Kalinin, S. V.; Ahmadi, M.; Ovchinnikova, O. S. Ferroic Halide Perovskite Optoelectronics. *Adv. Funct. Mater.* **2021**, *31* (36), 2102793.
(24) Dujana, W. A.; Podder, A.; Das, O.; Solayman, M.; Nasir, M. T.; Rashid, M. A.; Saiduzzaman, M.; Hadi, M. A. Structural, Electronic, Mechanical, Thermal, and Optical Properties of UIr3 under Pressure: A Comprehensive DFT Study. *AIP Advances* **2021**, *11* (10), 105205.
(25) Asrafusjaman, M.; Hasan, M.; Islam, M. A.; Hossain, A. K. M. A. Pressure-Induced Semiconductor-to-Metallic Transition of Monoclinic KCa2Nb3O10 Layered Perovskite: A Theoretical DFT Insight. *Crystal Research and Technology* **2023**, *58*, 2200262.
(26) Hadenfeldt, C.; Schulz, P. Darstellung, Struktur Und Temperaturabhängigkeit Der Phasenbreite Der Phase Ca2- XAs1- XBr1+ x Und Thermisches Verhalten Der Verbindung Ca3AsBr3. *Zeitschrift für anorganische und allgemeine Chemie* **1984**, *518* (11), 77−86.
(27) Li, Y.; Tongay, S.; Yue, Q.; Kang, J.; Wu, J.; Li, J. Metal to Semiconductor Transition in Metallic Transition Metal Dichalcogenides. *J. Appl. Phys.* **2013**, *114* (17), 174307.
(28) Afsari, M.; Boochani, A.; Hantezadeh, M. Electronic, Optical and Elastic Properties of Cubic Perovskite CsPbI3: Using First Principles Study. *Optik* **2016**, *127* (23), 11433−11443.
(29) Rahman, M. A.; Babu, M. M. H.; Karimunnesa, S.; Kholil, M. I. Properties of RbHgF3 Fluoro-Perovskite under Growing Hydrostatic Pressure from First-Principles Calculations. *AIP Advances* **2021**, *11* (11), 115201.
(30) Islam, M. A. U.; Islam, M. R.; Das, O.; Kato, S.; Kishi, N.; Soga, T. First-Principles Calculations to Investigate the Stability and Thermodynamic Properties of a Newly Exposed Lithium-Gallium-Iridium-Based Full-Heusler Compound. *ACS Omega* **2023**, *8* (24), 21885−21897.
(31) Azeem, M.; Qin, Y.; Li, Z.-G.; Li, W. Cooperative B-Site Octahedral Tilting, Distortion and A-Site Conformational Change Induced Phase Transitions of a 2D Lead Halide Perovskite. *Materials Chemistry Frontiers* **2021**, *5* (20), 7587−7594.
(32) Rahman, M. F.; Rahman, M. A.; Islam, M. R.; Ghosh, A.; Bashar Shanto, M. A.; Chowdhury, M.; Al Ijajul Islam, M.; Rahman, M. H.; Hossain, M. K.; Islam, M. A. Unraveling the Strain-Induced and Spin-Orbit Coupling Effect of Novel Inorganic Halide Perovskites of Ca3AsI3 Using DFT. *AIP Advances* **2023**, *13* (8), 085329.
(33) Rahman, M. F.; Islam, M. M.; Islam, M. R.; Ghosh, A.; Rahman, A.; Rahman, M. H.; Islam, M. A. I.; Islam, M. A.; Albalawi, H.; Mahmood, Q. An Investigation on Strain-Incited Electronic and Optical Properties of Novel Inorganic Cubic Material Sr3AsCl3. *J. Solid State Chem.* **2023**, *328*, 124341.
(34) Islam, M. R.; Mojumder, M. R. H.; Islam, A. S. M. J.; Alom, M. Z. Strain-Driven Tunability of the Optical, Electronic, and Mechanical Properties of Lead-Free Inorganic CsGeCl3 Perovskites. *Phys. Scr.* **2022**, *97* (12), 125817.
(35) Ghebouli, B.; Ghebouli, M. A.; Fatmi, M.; Bouhemadou, A. First-Principles Study of the Structural, Elastic, Electronic, Optical and Thermodynamic Properties of the Cubic Perovskite CsCdCl3 under High Pressure. *Solid state communications* **2010**, *150* (39−40), 1896−1901.
(36) Jain, Y.; Muneersab, S. S.; Shrivastava, D.; Kurchania, R. Structural, Mechanical, Electronic, Vibrational and Thermoelectric Properties of Novel Double Perovskites Ba2MgPdO6 and Ba2MgPtO6 within DFT Framework. *Materials Science in Semiconductor Processing* **2023**, *158*, 107381.
(37) Gillani, S. F.; Yasmin, N.; Usman, Z.; Khan, H. M.; Safdar, M.; Mirza, M. First Principles Study on Optical and Thermal Properties of BaTiS3. *Optik* **2022**, *261*, 169196.
(38) Green, M. A.; Jiang, Y.; Soufiani, A. M.; Ho-Baillie, A. Optical Properties of Photovoltaic Organic-Inorganic Lead Halide Perovskites. *journal of physical chemistry letters* **2015**, *6* (23), 4774−4785.
(39) Parr, R. G.; Yang, W. Density-Functional Theory of the Electronic Structure of Molecules. *Annu. Rev. Phys. Chem.* **1995**, *46* (1), 701−728.
(40) Ernzerhof, M.; Scuseria, G. E. Assessment of the Perdew-Burke-Ernzerhof Exchange-Correlation Functional. *J. Chem. Phys.* **1999**, *110* (11), 5029−5036.
(41) Clark, S. J.; Segall, M. D.; Pickard, C. J.; Hasnip, P. J.; Probert, M. I. J.; Refson, K.; Payne, M. C. First Principles Methods Using CASTEP. *Zeitschrift für kristallographie-crystalline materials* **2005**, *220* (5−6), 567−570.
(42) Milman, V.; Refson, K.; Clark, S. J.; Pickard, C. J.; Yates, J. R.; Gao, S.-P.; Hasnip, P. J.; Probert, M. I. J.; Perlov, A.; Segall, M. D. Electron and Vibrational Spectroscopies Using DFT, Plane Waves and Pseudopotentials: CASTEP Implementation. *Journal of Molecular Structure: THEOCHEM* **2010**, *954* (1−3), 22−35.
(43) Segall, M. D.; Lindan, P. J. D.; Probert, M. J. al; Pickard, C. J.; Hasnip, P. J.; Clark, S. J.; Payne, M. C. First-Principles Simulation: Ideas, Illustrations and the CASTEP Code. *J. Phys.: Condens. Matter* **2002**, *14* (11), 2717.
(44) Choudhary, K.; Tavazza, F. Convergence and Machine Learning Predictions of Monkhorst-Pack k-Points and Plane-Wave Cut-off in High-Throughput DFT Calculations. *Computational materials science* **2019**, *161*, 300−308.
(45) Monkhorst, H. J.; Pack, J. D. Special Points for Brillouin-Zone Integrations. *Phys. Rev. B* **1976**, *13* (12), 5188.
(46) Hadi, M. A.; Ali, M. S. New Ordered MAX Phase Mo2TiAlC2: Elastic and Electronic Properties from First-Principles. *Chinese Physics B* **2016**, *25* (10), 107103.
(47) Durham, B.; Dziedzic, J.; Hasnip, P.; Probert, M. *CASTEP Solvation Forces: eCSE01-09*; EPCC, 2022.
(48) Yang, Y.; Lu, H.; Yu, C.; Chen, J. M. First-Principles Calculations of Mechanical Properties of TiC and TiN. *J. Alloys Compd.* **2009**, *485* (1−2), 542−547.
(49) Islam, M. A.; Islam, M. R.; Rahaman, M. Z.; Soga, T. First-Principles Study of Physical, and Superconducting Properties of Newly Discovered Full-Heusler Compound MgPd2Sb. *Phys. Scr.* **2022**, *97* (12), 125705.
(50) Rahaman, M. Z.; Islam, M. A. A Theoretical Investigation on the Physical Properties of SrPd2Sb2 Superconductor. *Journal of Superconductivity and Novel Magnetism* **2021**, *34* (4), 1133−1139.
(51) Nam, S.; French, A. D.; Condon, B. D.; Concha, M. Segal Crystallinity Index Revisited by the Simulation of X-Ray Diffraction Patterns of Cotton Cellulose Iβ and Cellulose II. *Carbohydr. Polym.* **2016**, *135*, 1−9.
(52) Fu, H.; Li, D.; Peng, F.; Gao, T.; Cheng, X. Ab Initio Calculations of Elastic Constants and Thermodynamic Properties of NiAl under High Pressures. *Comput. Mater. Sci.* **2008**, *44* (2), 774−778.
(53) Zener, C. M.; Siegel, S. Elasticity and Anelasticity of Metals. *J. Phys. Chem.* **1949**, *53* (9), 1468.
(54) Ledbetter, H.; Migliori, A. A General Elastic-Anisotropy Measure. *Journal of applied physics* **2006**, *100* (6), 63516.
(55) Greaves, G. N.; Greer, A. L.; Lakes, R. S.; Rouxel, T. Poisson's Ratio and Modern Materials. *Nature materials* **2011**, *10* (11), 823−837.
(56) Islam, M. R.; Mojumder, M. R. H.; Moshwan, R.; Islam, A. S. M. J.; Islam, M. A.; Rahman, M. S.; Kabir, M. H. Strain-Driven Optical, Electronic, and Mechanical Properties of Inorganic Halide Perovskite CsGeBr3. *ECS Journal of Solid State Science and Technology* **2022**, *11* (3), 033001.
(57) Islam, M. A.; Islam, J.; Islam, M. N.; Sen, S. K.; Hossain, A. K. M. A. Enhanced Ductility and Optoelectronic Properties of Environment-Friendly CsGeCl3 under Pressure. *AIP Advances* **2021**, *11* (4), 045014.
(58) Eberhart, M. E.; Jones, T. E. Cauchy Pressure and the Generalized Bonding Model for Nonmagnetic Bcc Transition Metals. *Phys. Rev. B* **2012**, *86* (13), 134106.
(59) Combes, J.-M.; Duclos, P.; Seiler, R. The Born-Oppenheimer Approximation. In *Rigorous Atomic and Molecular Physics*; Springer, 1981; pp 185−213.
(60) Pugh, S.F. XCII. Relations between the Elastic Moduli and the Plastic Properties of Polycrystalline Pure Metals. *London, Edinburgh,*

https://doi.org/10.1021/acsomega.3c08131
ACS Omega 2024, 9, 8005−8018

and Dublin Philosophical Magazine and Journal of Science **1954**, *45* (367), 823−843.
(61) Islam, R.; Islam, S.; Mojumder, R. H.; Khan, Z.; Molla, H.; Islam, A. S. M. J.; Park, J. Tuning the Electronic, Phonon, and Optical Properties of Monolayer BX (XP and As) through the Strain Effect. *Mater. Today Commun.* **2022**, *33*, 104227.
(62) Khan, M.; Rahaman, M. Z.; Ali, M. L. Pressure-Induced Band Gap Engineering of Nontoxic Lead-Free Halide Perovskite CsMgI3 for Optoelectronic Applications. *ACS Omega* **2023**, *8* (28), 24942−24951.
(63) Gaillac, R.; Pullumbi, P.; Coudert, F.-X. ELATE: An Open-Source Online Application for Analysis and Visualization of Elastic Tensors. *J. Phys.: Condens. Matter* **2016**, *28* (27), 275201.
(64) Ranganathan, S. I.; Ostoja-Starzewski, M. Universal Elastic Anisotropy Index. *Physical review letters* **2008**, *101* (5), 55504.
(65) Kube, C. M.; De Jong, M. Elastic Constants of Polycrystals with Generally Anisotropic Crystals. *J. Appl. Phys.* **2016**, *120* (16), 165105.
(66) Polman, A.; Knight, M.; Garnett, E. C.; Ehrler, B.; Sinke, W. C. Photovoltaic Materials: Present Efficiencies and Future Challenges. *Science* **2016**, *352* (6283), 44241−442410.
(67) Sai, N.; Zwolak, M.; Vignale, G.; Di Ventra, M. Dynamical Corrections to the DFT-LDA Electron Conductance in Nanoscale Systems. *Physical review letters* **2005**, *94* (18), 186810.
(68) Aryasetiawan, F.; Gunnarsson, O. The GW Method. *Rep. Prog. Phys.* **1998**, *61* (3), 237.
(69) Yang, J.; Tan, L. Z.; Rappe, A. M. Hybrid Functional Pseudopotentials. *Phys. Rev. B* **2018**, *97* (8), 85130.
(70) Peralta, J. E.; Heyd, J.; Scuseria, G. E.; Martin, R. L. Spin-Orbit Splittings and Energy Band Gaps Calculated with the Heyd-Scuseria-Ernzerhof Screened Hybrid Functional. *Phys. Rev. B* **2006**, *74* (7), 73101.
(71) Jain, A.; Hautier, G.; Ong, S. P.; Moore, C. J.; Fischer, C. C.; Persson, K. A.; Ceder, G. Formation Enthalpies by Mixing GGA and GGA+ U Calculations. *Phys. Rev. B* **2011**, *84* (4), 45115.
(72) Aslam, M.; Khan, A.; Hashmi, M. A.; Sajjad, M.; Algrafy, E.; Mustafa, G. M.; Mahmood, A.; Ramay, S. M. Physical Characteristics of CdZrO3 Perovskite at Different Pressure for Optoelectronic Application. *Journal of Materials Research and Technology* **2020**, *9* (5), 9965−9971.
(73) Gillani, S.S.A.; Ahmad, R.; Zeba, I.; Islah-u-din; Shakil, M.; Rizwan, M.; Rafique, M.; Sarfraz, M.; Hassan, S.S. Effect of External Pressure on the Structural Stability, Electronic Structure, Band Gap Engineering and Optical Properties of LiNbO3: An Ab-Initio Calculation. *Mater. Today Commun.* **2020**, *23*, 100919.
(74) Kholil, M. I.; Bhuiyan, M. T. H. Effects of Pressure on Narrowing the Band Gap, Visible Light Absorption, and Semi-Metallic Transition of Lead-Free Perovskite CsSnBr3 for Optoelectronic Applications. *J. Phys. Chem. Solids* **2021**, *154*, 110083.
(75) Noor, N. A.; Mahmood, Q.; Rashid, M.; Ul Haq, B.; Laref, A. The Pressure-Induced Mechanical and Optoelectronic Behavior of Cubic Perovskite PbSnO3 via Ab-Initio Investigations. *Ceram. Int.* **2018**, *44* (12), 13750−13756.
(76) Arif, H.; Tahir, M. B.; Almutairi, B. S.; Khalid, I.; Sagir, M.; Elhosiny Ali, H.; Alrobei, H.; Alzaid, M. CASTEP Study for Mapping Phase Stability, and Optical Parameters of Halide Perovskite CsSiBr3 for Photovoltaic and Solar Cell Applications. *Inorg. Chem. Commun.* **2023**, *150*, 110474.
(77) Khan, K.; Sahariya, J.; Soni, A. Structural, Electronic and Optical Modeling of Perovskite Solar Materials ASnX3 (A= Rb, K; X= Cl, Br): First Principle Investigations. *Mater. Chem. Phys.* **2021**, *262*, 124284.
(78) Xu, Z. The Determination of the Momentum Matrix Elements Involved in Calculating the Dielectric Constants of Superlattices Using the Tight-Binding Method. *Solid state communications* **1990**, *76* (9), 1143−1147.
(79) Rajeswarapalanichamy, R.; Amudhavalli, A.; Padmavathy, R.; Iyakutti, K. Band Gap Engineering in Halide Cubic Perovskites CsPbBr3- YIy (Y= 0, 1, 2, 3)-A DFT Study. *Materials Science and Engineering: B* **2020**, *258*, 114560.

https://doi.org/10.1021/acsomega.3c08131
ACS Omega 2024, 9, 8005−8018